Draft version March 4, 2024
Preprint typeset using LaTeX style emulateapj v. 5/2/11

MAGNETAR OUTBURSTS FROM AVALANCHES OF HALL WAVES AND CRUSTAL FAILURES

Xinyu Li[1], Yuri Levin[2,1] and Andrei M. Beloborodov[1]
[1]Physics Department and Columbia Astrophysics Laboratory, Columbia University, 538 West 120th Street, New York, NY 10027 and
[2]School of Physics and Astronomy, Monash University, Clayton, VIC 3800, Australia
Draft version March 4, 2024

ABSTRACT

We explore the interaction between Hall waves and mechanical failures inside a magnetar crust, using detailed one-dimentional models that consider temperature-sensitive plastic flow, heat transport and cooling by neutrino emission, as well as the coupling of the crustal motion to the magnetosphere. We find that the dynamics is enriched and accelerated by the fast, short-wavelength Hall waves that are emitted by each failure. The waves propagate and cause failures elsewhere, triggering avalanches. We argue that these avalanches are the likely sources of outbursts in transient magnetars.

Subject headings: dense matter — magnetic fields — stars: magnetars — stars: neutron — waves

1. INTRODUCTION

Magnetars are luminous slowly rotating neutron stars that are thought to be powered by the decay of ultra-strong magnetic fields $B = 10^{14} - 10^{16}$G (see e.g. Woods & Thompson (2006); Mereghetti (2008) for reviews). They have hot surfaces and produce hard X-rays flares as well as persistent nonthermal magnetospheric radiation. So-called transient magnetars show periods of low luminosity followed by months-to-years long outbursts, increasing X-ray luminosity by up to 3 orders of magnitude (Ibrahim et al. 2004; Gotthelf et al. 2004; Mereghetti 2008; Rea & Esposito 2011).

The mechanism triggering this activity is not established. Following the original ideas of Thompson & Duncan (1996), Perna & Pons (2011) argued that the outbursts are powered by localized releases of elastic energy in the crust due to mechanical failures in the crystal lattice (the "starquakes"). They modeled the build up of the elastic energy before each release as a result of the changing magnetic stresses, and have produced a phenomenological numerical model for the frequency of the outbursts and the magnitude of their energy release. Pons & Rea (2012) have modeled the outbursts by computing the thermal flux emerging from the neutron star surface from an impulsive energy release in the crust (see Kaminker et al. (2006, 2014) for a detailed discussion of heat transfer through the magnetar's crust).

The magnetic field in the crust evolves due to a combined action of the Hall drift and ohmic dissipation (Goldreich & Reisenegger 1992; Hollerbach & Rüdiger 2004; Viganò et al. 2013). The multi-dimensional dynamics of the Hall drift in the neutron-star crust is complex and not fully understood, although significant new insights have come from recent numerical experiments (Kojima & Kisaka 2012; Gourgouliatos et al. 2013; Gourgouliatos & Cumming 2014, 2015; Wood & Hollerbach 2015). It is generally thought to proceed on long timescales of $\sim 10^3$ years in the deep crust.

The gradual evolution of the magnetic field due to Hall drift is punctuated by shearing motions of the crust that relieve magnetic stresses. Beloborodov & Levin (2014) proposed that these yielding motions occur through transient thermoplastic waves, which resemble deflagration fronts burning magnetic energy. These fronts leave sharp gradients in the crustal magnetic fields, which must feedback on the field evolution through Hall drift. The goal of the present paper is to explore the interaction between the Hall evolution and the mechanical failures that such evolution induces. We show that each failure produces a burst of short Hall waves which speed up the evolution. The short Hall waves propagate to different parts of the crust and cause new mechanical failures, thus producing an avalanche. We propose that these avalanches are the mechanism of outbursts in transient magnetars.

We build a detailed one-dimensional model which follows the following processes:
1. Rapid plastic motions driven by super-critical magnetic stresses, and the associated emission of short Hall waves.
2. Transport of the generated plastic heat and neutrino cooling of the crust. This allows us to find the thermal flux emitted from the stellar surface.
3. Surface shear resulting from the crustal avalanches, and the associated Poynting flux into the magnetosphere. This flux can feed a magnetospheric activity.

The plan of the paper is as follows. Sections 2-4 describe the mechanism of Hall-wave generation, plastic failures, and the crustal failure development through the Hall-mediated avalanche. Section 5 introduces a simplified model of magnetospheric twisting by the crustal failures that is adapted for one-dimensional simulations. Section 6 presents a numerical simulation of the 10-kyr evolution of the crustal magnetic field coupled to the magnetosphere. Connections of the model to observations are discussed in Section 7.

2. HALL WAVES

The magnetic field evolution in the crust is governed by the equation

$$\dot{\boldsymbol{\mathcal{B}}} = \nabla \times (\boldsymbol{v} \times \boldsymbol{\mathcal{B}}) + \nabla \times (\eta \nabla \times \boldsymbol{\mathcal{B}}) \,. \tag{1}$$

Hereafter dot above a symbol signifies time derivative $\partial/\partial t$. The first term on the right-hand side represents advection of the magnetic field by the electron fluid, which is moving with velocity $\boldsymbol{v}$ in the frame of undeformed crust, and the second term represents ohmic diffusion,

with the diffusivity given by

$$\eta = \frac{c^2}{4\pi\gamma}, \tag{2}$$

where γ is the electrical conductivity of the crust. The electron velocity consists of three components:

$$\boldsymbol{v} = \boldsymbol{v}_{\rm H} + \dot{\boldsymbol{\xi}}_{\rm ela} + \dot{\boldsymbol{\xi}}_{\rm pl}. \tag{3}$$

Here $\boldsymbol{v}_H$ is the Hall drift velocity; it describes the electron motion relative to the ions and is related to the electric current density $\boldsymbol{j}$,

$$\boldsymbol{v}_H = -\frac{\boldsymbol{j}}{n_e e} = -\frac{c}{4\pi n_e e}\nabla\times\boldsymbol{\mathcal{B}}, \tag{4}$$

where n_e is the electron density and $-e$ is the electron charge. The other two terms on the right-hand side of Equation (3) represent the motion of the ions; $\boldsymbol{\xi}_{\rm ela}$ is the elastic deformation of the lattice and $\boldsymbol{\xi}_{\rm pl}$ is the plastic deformation. The ion motion was neglected in all studies of the Hall evolution of the crustal magnetic field except the work of Cumming et al. (2004), who discussed the contribution of $\boldsymbol{\xi}_{\rm ela}$ to the field dynamics and showed that it dramatically changes the dispersion relation of Hall waves in the upper layers of the crust.

Similar to Cumming et al. (2004), we consider a simplified plane-parallel configuration with the vertical z axis pointing from the core to the surface. [1] The ion lattice displacement $\boldsymbol{\xi} = \boldsymbol{\xi}_{\rm ela} + \boldsymbol{\xi}_{\rm pl}$ is purely horizontal, and the model is one-dimensional in the sense that all variables (magnetic field, displacement, temperature, conductivity, etc.) are functions of z and time t. Then $\boldsymbol{\mathcal{B}}(z,t) = (B_x, B_y, B_z)$ has a constant B_z component, and the evolution equation for the horizontal field reduces to

$$\dot{B}_a = B_z\partial_z\left[v_{H,a} + \dot{\xi}_a\right] + \partial_z\left(\eta\partial_z B_a\right), \tag{5}$$

where index $a = x, y$ corresponds to the horizontal components. It is convenient to define a complex-valued magnetic field $B \equiv B_x + iB_y$, displacement $\xi \equiv \xi_x + i\xi_y$, etc. Then

$$v_H \equiv v_{H,x} + iv_{H,y} = -i\frac{c}{4\pi n_e e}\partial_z B, \tag{6}$$

and the evolution equations reads

$$\dot{B} = -i\partial_z\left(D\partial_z B\right) + B_z\partial_z\dot{\xi}. \tag{7}$$

Here $D = D_H + i\eta$, and the Hall diffusion coefficient is

$$D_H = \frac{B_z c}{4\pi n_e e}. \tag{8}$$

2.1. *Generation of Hall waves*

In this paper we will explore two processes that can produce Hall waves in the crust. First, Thompson & Duncan (1996) argued that a sudden rearrangement of magnetic field lines in the core can launch Hall waves from the core-crust interface into the crust. Fast magnetic rearrangement due to hydromagnetic instability during the early life of the magnetar or rapid ambipolar diffusion in the hot magnetar core (Goldreich & Reisenegger 1992; Beloborodov & Li 2016) can create a current sheet at the core-crust interface. Configurations with the current sheet at the interface was considered by **??** in the context of superconducting stars, and also appeared in some simulations of the core field expulsion (**?**). This localized horizontal current drags the field lines and launches a train of Hall waves that propagate toward the top of the crust. More importantly, local sudden mechanical failures in the crust can induce a local change in the horizontal magnetic field. This change generates horizontal currents that drag the field lines and launch Hall waves which propagate both upward and downward from the failure.

[1] In our simplified 1D model the Hall evolution term is linear; the non-linearity enters into our model through the yielding of the crust to magnetically-induced stresses.

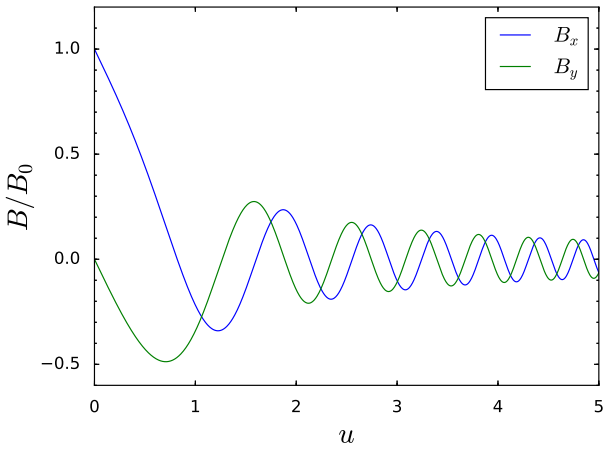

FIG. 1.— Self-similar wave $B_x(u)$, $B_y(u)$ (where $u = z/\sqrt{2D_H t}$) in a homogeneous crust of infinite conductivity with the initial $B = B_x + iB_y = 0$. The wave is launched at $t = 0$ and $z = 0$ by the jump of B_x from 0 to B_0. $B_x = B_0$ is kept fixed at the boundary $z = 0$ while the Hall evolution of $B(z,t)$ washes out the jump with time. The constant profile $B(u)$ implies the self-similar stretching of $B(z)$ as $z \propto t^{1/2}$, from initially infinitesimal to arbitrary large widths.

It is instructive to consider first a simple analytical example of how a burst of Hall waves is generated; this example was studied by Lyutikov (2015) in a different context. In this example the crust is a homogeneous, infinitely rigid, ideal conductor (these assumptions will be relaxed below). The field evolution equation then becomes

$$\dot{B} + iD_H\partial_z^2 B = 0. \tag{9}$$

This equation admits simple wave solutions with the dispersion relation $\omega = D_H k^2$. Note that shorter waves (large wavenumbers k) have higher phase speeds ω/k and group speeds $2\omega/k$. The Green's function $G(z,z';t)$ for Equation (9) is given by

$$G(z,z';t) = \frac{1}{\sqrt{-4\pi i D_H t}}\exp\left[-i\frac{(z-z')^2}{4D_H t}\right]. \tag{10}$$

Given an initial condition $B(z,0)$ one can find the solution,

$$B(z,t) = \int \mathrm{d}z'\, G(z,z';t)B(z',0). \tag{11}$$

Let us consider the initial condition $B(z,0) = 0$ everywhere in the crust except its boundary with the core, where the field jumps to $B_0 \neq 0$. The boundary condition is fixed at B_0 throughout the evolution. Then the

solution is given by

$$\frac{B(z,t)}{B_0} = 1 - \sqrt{\frac{2}{\pi}}\frac{2}{1-i}\left[\mathcal{C}(u) - i\mathcal{S}(u)\right], \qquad (12)$$

where $u = z/\sqrt{4D_H t}$; $\mathcal{S}$ and $\mathcal{C}$ are Fresnel integrals,

$$\mathcal{S}(u) = \int_0^u \sin(s^2)\,\mathrm{d}s, \quad \mathcal{C}(u) = \int_0^u \cos(s^2)\,\mathrm{d}s. \qquad (13)$$

The solution is self-similar; its dependence on u is shown in Figure 1. It demonstrates how the horizontal current sheet at the boundary generates a broad spectrum of Hall waves. The fast short waves lead the longer waves.

The same problem with a realistic density profile $\rho(z)$ and electric conductivity $\gamma(z)$ can be solved numerically using Equation (7) (neglecting crustal deformation ξ). The finite resistivity leads to efficient damping of the fast Hall waves with high wavenumbers, limiting the speed of the wavefront launched by the jump of B_x. Figure 2 shows four snapshots of the resulting evolution of the magnetic field.

Similar waves will be launched by a plastic flow that has created a jump in B at some $z_0 > 0$ inside the crust, as will be discussed below. In this case, one will need to trace the crustal Hall waves excited at $z < z_0$ and $z > z_0$.

3. PLASTIC FAILURES

3.1. *Stress balance*

Hall evolution can generate strong shear stresses $BB_z/4\pi$, where B is the horizontal magnetic field. As long as the external $B = 0$ at the top of the crust (this assumption will be relaxed in Section 5) the stress balance is only possible if the entire stress $BB_z/4\pi$ is offset by the elastic stress of the ion lattice,

$$\frac{BB_z}{4\pi} = -\mu\,\partial_z \xi_{\rm ela} = \sigma, \qquad (14)$$

where μ is the shear modulus of the lattice. We expect the stress balance to be satisfied to a high precision at all times, even during a crustal failure when a plastic flow occurs (Beloborodov & Levin 2014), provided that the plastic flow is slow compared with the relaxation to stress balance. The latter occurs on the shear-sound-crossing timescale <0.1 s.

Taking the time derivative on both sides of Equation (14) and substituting into Equation (7), we get

$$\left(1 + \frac{\mu_B}{\mu}\right)\dot{B} = -i\partial_z\left(D\partial_z B\right) + B_z\partial_z\dot{\xi}_{\rm pl}, \qquad (15)$$

where $\mu_B \equiv B_z^2/4\pi$. The above equation, but without the plastic deformation term on the right-hand side, was derived and used to obtain the dispersion relation of Hall waves in Cumming et al. (2004). The elastic deformation of the crust strongly affects the Hall-wave propagation when $\mu < \mu_B$.

3.2. *Mechanical failure*

When the shear stress in the crust reaches a critical value

$$\sigma_{\rm cr} \sim 0.1\mu, \qquad (16)$$

the crust must yield inelastically, as demonstrated in numerical experiments by Horowitz & Kadau (2009) and Chugunov & Horowitz (2010). They propose that $\sigma_{\rm cr}$ depends on temperature as

$$\sigma_{\rm cr}(T) = \sigma_{\rm cr}(0)\left(1 - \frac{65.128}{\Gamma - 71}\right), \qquad (17)$$

where $\Gamma = Z^2e^2/akT$ is the Coulomb coupling parameter for ions with charge number Z and separation $a = (3/4\pi n_{\rm i})^{1/3}$ ($n_{\rm i}$ is the ion number density.) These authors studied rapidly shearing boxes of $\sim 100\times100\times100$ lattice sites, and found that after the shear stress reaches $\sim 0.1\mu$ the failure develops with the stress reduced by an order of magnitude. When the shear ends, the crystal strength must eventually heal. Our model below will assume a similar behavior of the elastic stress in macroscopic failure events, although the extrapolation of the small-scale rapid-shear experiments to slowly fostered macroscopic failures may not be reliable. Note also that two-dimensional shear failures, common in the earth crust as sources of earthquakes, are strongly suppressed in a magnetar by magnetic tension (Levin & Lyutikov 2012). The failure may be described as a plastic flow (Beloborodov & Levin 2014), see also Jones (2003).

The critical stress $\sigma_{\rm cr}$ defines the critical magnetic field $B_{\rm cr}$,

$$\frac{B_{\rm cr}B_z}{4\pi} = \sigma_{\rm cr}. \qquad (18)$$

Motivated by the results of Horowitz & Kadau (2009) we will assume that once the failure is initiated the critical stress drops to $\sigma_{\rm cr}^{\rm new} = 0.1\sigma_{\rm cr}$. Correspondingly, $B_{\rm cr}^{\rm new} = 0.1B_{\rm cr}$ during the plastic flow. This prescription makes sure that the horizontal magnetic field evolves to the lower value $B_{\rm cr}^{\rm new}$ in a visco-elastic manner. Once the elastic stress reaches $\sigma_{\rm cr}^{\rm new}$ we assume that the lattice reforms and the visco-elastic evolution stops. Our results are not sensitive to the exact choice of $\sigma_{\rm cr}$.

Finally, we specify the plastic flow rate (the last term in Equation (15)) using a simple viscoelastic model,

$$B_z\partial_z\dot{\xi}_{\rm pl} = -\alpha B\left(1 - \frac{B_{\rm cr}^{\rm new}}{|B|}\right)\Theta\left(|B| - B_{\rm cr}^{\rm new}\right). \qquad (19)$$

Here $\Theta(...)$ is the Heaviside step function, so the plastic flow occurs as long as $|B| > B_{\rm cr}^{\rm new}$. Equation (19) describes a shear failure motion that relaxes the local magnetic stress by driving the field B from $B_{\rm cr}$ to $B_{\rm cr}^{\rm new}$. The parameter α has the dimension of s^{-1} and determines the relaxation rate. After time $\tau \gg \alpha^{-1}$ from the beginning of the plastic failure, B becomes exponentially close to $B_{\rm cr}^{\rm new}$ and the crystal should heal, i.e. the critical stress should increase back to $\sigma_{\rm cr} \sim 0.1\mu$, ending the plastic flow. The qualitative results of this paper were found to be weakly affected by the choice of rate α and healing time τ for reasonably fast plastic flow rates. In the simulations presented below we use $\alpha = 10^{-4}$ s^{-1} and $\tau = 1$ yr.

3.3. *Heat transfer and thermoplastic waves*

The energy density that can be dissipated through plastic failures is the sum of magnetic and elastic en-

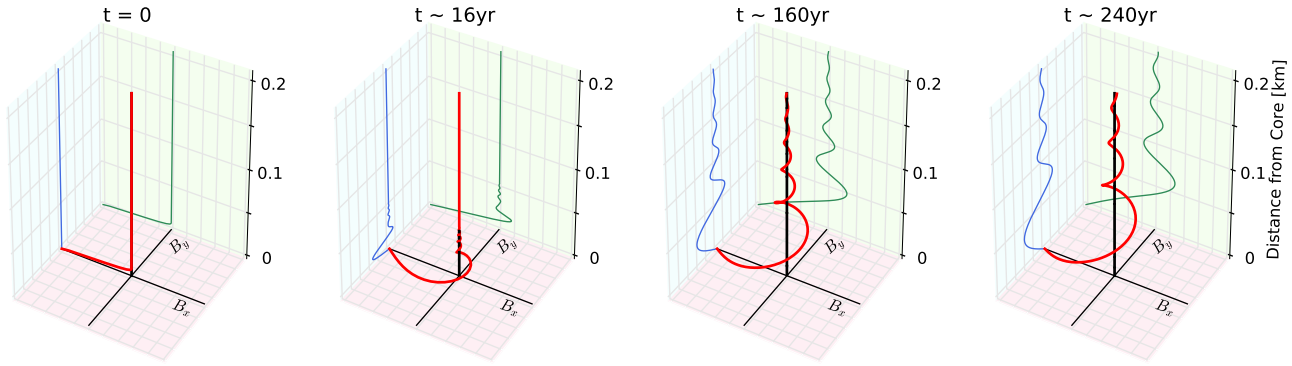

FIG. 2.— Generation of Hall waves by a jump of B_x from $B_x = 0$ at $z \gtrsim 10$ m to $B_x = B_0 = 6\times10^{15}$ G at $z = 0$ (the core-crust interface). The four snapshots show the evolution of B_x and B_y; vertical field $B_z = 3\times10^{14}$ G remains constant. The evolution is calculated using a realistic density profile $\rho(z)$ and conductivity $\gamma(z)$ of the crust. The black lines indicate the x, y, z axes. The red curve traces the end of the horizontal vector (B_x, B_y), which is a function of the vertical position z. The green and blue projections show $B_x(z)$ and $B_y(z)$; they resemble the self-similar solution shown in Figure 1.

ergies,

$$U = \frac{|B|^2}{8\pi} + \frac{1}{2}\mu|\partial_z\xi_{\rm ela}|^2 = \left(1+\frac{\mu_B}{\mu}\right)\frac{|B|^2}{8\pi}. \quad (20)$$

The dissipation rate due to plastic flow is given by

$$q_{\rm pl} = \frac{B_z\left|B\partial_z\dot{\xi}_{\rm pl}\right|}{4\pi}, \quad (21)$$

where $|B| = (B_x^2 + B_y^2)^{1/2}$.

Beloborodov & Levin (2014) showed that the temperature-softening effect, i.e. the reduction of $\sigma_{\rm cr}(T)$ with increasing T, allows the plastic failure to propagate through heat diffusion. The resulting thermoplastic wave (TPW) resembles a deflagration front, and its speed is

$$v \sim (\alpha\chi)^{1/2}, \quad (22)$$

where $\chi = \kappa/C_V \sim 10-100$ cm^2 s^{-1} is the heat diffusion coefficient, with C_V and κ being the heat capacity and thermal conductivity of the crustal material. The TPWs are much faster than the Hall waves, so the Hall evolution is negligible during the crustal failure through a TPW.

The TPW propagation requires that the magnetic field ahead of the wave B_0 be sufficiently close to $B_{\rm cr}$, so that heat diffusion from the plastic flow is capable of reducing $B_{\rm cr}(T)$ below B_0. A simple propagating solution $B(z-vt)$ is obtained from Equation (19) assuming a uniform medium ahead of the wave with a uniform field B_0. Suppose the wave was launched at $z_\star$ at time $t_\star$. In the plastically flowing region $z - vt < z_\star - vt_\star$, Equation (19) gives

$$-v\frac{dB}{dw} = -\alpha B\left(1-\frac{B_{\rm cr}^{\rm new}}{|B|}\right), \qquad w = z - vt. \quad (23)$$

Then one finds the solution,

$$B = (B_0 - B_1)\exp\left[\frac{\alpha}{v}(w - w_\star)\right] + B_0, \quad w < w_\star, \quad (24)$$

which describes the plastic relaxation of B_0 to a weaker field $|B_1| = B_{\rm cr}^{\rm new}$. One can see that the characteristic thickness of the wave front is v/α.

A TPW launched in a non-uniform background will eventually extinguish, leaving a jump of the magnetic field $B_0 \to B_1$ of width $\sim v/\alpha$. This jump affects the subsequent Hall evolution of the magnetic field.

4. HALL-MEDIATED AVALANCHE

The jumps of the horizontal magnetic field as a result of plastic failures generate Hall waves. This can be illustrated by an idealized model of a homogeneous crust with an initially uniform field B_0 that was suddenly changed to $B_1 = 0.1B_0$ at $z < z_0$. $|B_1| = B_{\rm cr}^{\rm new}$ carries the same meaning as in Equation (24). The problem is similar to that considered in Section 2 except that now B jumps from B_0 to B_1 at z_0 instead of jumping from B_0 to 0 at $z = 0$.

The analytical solution for the Hall evolution caused by the jump is given by

$$B(z,t) = B_1 + \frac{(8/\pi)^{1/2}}{1-i}\left[\mathcal{C}(u) - i\mathcal{S}(u)\right](B_0 - B_1), \quad (25)$$

where $u = (z - z_0)/\sqrt{4D_H(t-t_0)}$ and t_0 is the initial time at which the jump was created. Snapshots of this solution at $z > z_0$ are shown in Figure 3. This solution is similar to Equation (12), but with different boundary conditions. The peaks of the oscillating profile are moving from left to right and their widths increase with time as $t^{1/2}$. In the idealized problem, where the infinitely sharp jump is created instantaneously, the peaks start out infinitesimally narrow. More realistically, the jump is implanted at the end of a plastic failure in a finite time $\delta t \sim \alpha^{-1}$. This timescale determines the characteristic peak width at the beginning of the evolution. At times $t - t_0 \gg \delta t$ the evolution becomes self-similar and accurately described by Equation (25).

A key feature is that *the peaks of the launched Hall waves significantly exceed the background field* B_0. The

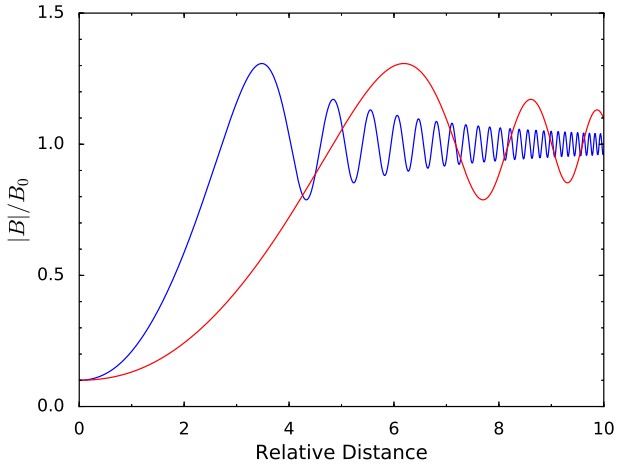

FIG. 3.— Profile of the horizontal magnetic field $|B|$ at two different times, according to the self-similar solution given by Equation (25). The peaks are moving from left to right.

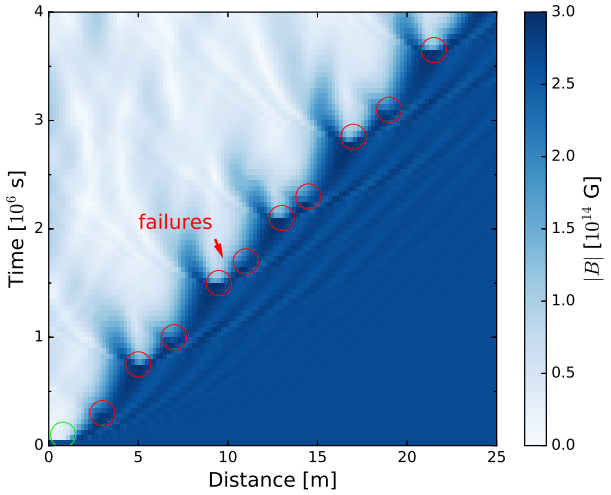

FIG. 4.— Numerical simulation demonstrating the Hall-mediated failure of the crust (see text). A seed plastic failure is initiated at $t = 0$ and $z < 2$ m; it is indicated by the green circle on the spacetime diagram. Magnetic field $|B|$ is quickly reduced in the failed region, so it becomes white (weak field) according to the color code indicated next to the diagram. The failed region is expanding due to the short Hall waves launched by the plastic flows into the intact region, where the waves trigger new plastic flows.

highest peak is $1.3B_0$. This implies that the Hall waves are capable of breaking the crust and inducing new plastic flows, leading to an avalanche of plastic failures. [2]

The avalanche development can be demonstrated by the following numerical experiment. Consider a uniform crust with electron density $n_e = 10^{35}$ cm^{-3} and $B_z = 3 \times 10^{14}$ G; this gives the Hall diffusion coefficient $D_H \approx 0.015$ cm^2 s^{-1}. To isolate the effect of interest we turn off heat diffusion, so there will be no TPWs, and new plastic flows can only be induced by Hall waves. As an initial condition at $t = 0$ we take a uniform field $|B_0| = 2.7 \times 10^{14}$ G. We set $B_{\rm cr} = 3 \times 10^{14}$ G everywhere except a small region $|z - z_0| < 2$ m. In this region, we trigger the plastic flow by setting $B_{\rm cr}^{\rm new} = 0.1 B_{\rm cr}$. This setup is designed to produce an initially localized plastic flow, which reduces the field in the small region and launches Hall waves. Our experiment follows the evolution by solving the Hall equation (15) and simulating any new plastic flows, which must be triggered wherever $|B|$ exceeds $B_{\rm cr}$.

The result is convenient to view on the spacetime digram (Figure 4) that shows the evolution of $|B|$ in the region $z > z_0$. As expected, the peaks of launched Hall waves break the crust, creating new plastic flows. These flows generate new jumps in B, which create new Hall waves etc., expanding the region where the crust has failed. The average speed of the failed region expansion is determined by the slope of the boundary $z_{\rm front} \approx vt$ observed on the diagram. The magnetic field $|B|$ has been reduced (and magnetic energy has been dissipated) in the region $z < z_{\rm front}$. In contrast, in the region $z > z_{\rm front}$, the field is only perturbed by the faster and weaker Hall waves, which are seen as the propagating oscillations. The front speed is $v \approx 5.5 \times 10^{-4}$ cm/s, about half of $(\alpha D_H)^{1/2} = 1.2 \times 10^{-3}$ cm/s — the characteristic speed of Hall waves launched by plastic flows. As a rough estimate one can use

$$v \sim (\alpha D_H)^{1/2}. \qquad (26)$$

In essence, we observe a *Hall-mediated mode of crustal failure* (HMF). It is much slower than the heat-mediated TPW, however it can operate where TPWs do not propagate.

The HMF expansion occurs with no clean separation of the timescales of Hall and plastic evolution — the frequencies of excited Hall waves are comparable to α^{-1}. Therefore, the details of failure propagation are complicated. In particular, we observe a curious limit-cycle behavior: a fast reduction of $|B|$ on the timescale α^{-1} is followed by a failure event with a slower reduction of $|B|$ in a smaller region; then it takes a long time to trigger a new failure which again turns out fast and strong, closing the cycle.

The cycle is explained as follows. A fast failure launches a Hall wave with a narrow peak, $\delta z \sim (D_H/\alpha)^{1/2}$, and therefore the next plastic flow triggered by this peak occurs promptly and in a narrow region.[3] The relaxation of $|B|$ to $B_{\rm cr}^{\rm new} = 0.1 B_{\rm cr}$ in the narrow plastic region is hindered by the Hall-wave transport of magnetic energy — the locally dissipated magnetic en-

[2] While we believe that this effect will also be present in multi-dimensional configurations, geometry and non-linearities present in multi-dimension can change it quantitatively

[3] Plastic flow is initiated where the growing peak touches $B_{\rm cr}$, and the width of the induced failure is controlled by the curvature of $|B(z)|$ at the peak. In a complete model, with heat diffusion, a local TPW is produced, which quickly extinguishes as it propagates away from the peak. The model with switched off heat diffusion does not generate TPWs; instead, it generates a cascade of very thin plastic flows (limited by the grid resolution of 2 cm), which merge with time. Thus, the behavior on the smallest scales cannot be resolved in the simulation presented in Figure 4. However, the small-scale details weakly affect the behavior of the front on scales well above the grid scale — it turns out similar to a more complete simulation with included heat diffusion.

ergy is replenished by the Poynting flux

$$F_p = \frac{1}{8\pi} i D_H (B^* \partial_z B - B \partial_z B^*) = \frac{1}{4\pi} D_H (B_y \partial_z B_x - B_x \partial_z B_y) \quad (27)$$

into the plastic region, which resists the development of a localized sharp drop in $|B|$. The delay in the drop of $|B|$ causes a delay in the launching of a new super-critical Hall wave into the intact region ahead of $z_{\rm front}$. As a result the next failure event at $z > z_{\rm front}$ is delayed. When it finally occurs the wave peak is broad and triggers a plastic flow in a relatively broad region. The relaxation $|B| \to B_{\rm cr}^{\rm new}$ in the broad region is not hindered by the Poynting flux and occurs promptly, on the timescale of $\sim \alpha^{-1}$.

The limit cycle can be clearly seen in Figure 4 as the repeating appearance of "fingers" and fast failures. A "finger" pattern (e.g. one near distance 4 m and time 10^6 s) contains narrow failures separated by intact regions. Magnetic energy is only dissipated at narrow failure sites, and the Poynting flux from intact regions replenishes the energy there. It takes longer for $|B|$ to drop below $B_{\rm cr}^{\rm new}$ in the "finger" compared to fast failures to the right. After a fast failure in a broad region, new narrow failures are reproduced. Therefore the "finger" appears again.

We also performed simulations similar to that shown in Figure 4 that included heat diffusion and ohmic dissipation with a realistic $\eta \sim D_H/20$. We observed a similar propagation of the failure front, but with gradually damped peaks of the Hall waves. We also varied $|B_0|/B_{\rm cr}$ and found that when this ratio is closer to unity, the TPW becomes the dominant mode of failure propagation. It propagates much faster, with the velocity $v_{\rm TPW} \sim (\alpha\chi)^{1/2}$ well above the velocity of the Hall-mediated failure $v_{\rm HMF} \sim (\alpha D_H)^{1/2}$. Both failure modes will be seen to occur in the magnetar crust simulated in Section 6.

5. TWISTED EXTERNAL FIELD

The crustal motions must twist the external magnetosphere attached to the crust. Such external twists are observed in persistent magnetars through their hard X-ray emission (**?**Hascoët et al. 2014). In transient magnetars, evidence for magnetospheric twists is provided by shrinking hot spots on the stellar surface (Beloborodov 2009).

The external twist implies a non-zero horizontal magnetic field at the stellar surface $B_s \neq 0$. This changes the stress balance inside the crust, which now reads

$$\frac{\tilde{B} B_z}{4\pi} = -\mu \partial_z \xi_{\rm ela}, \qquad \tilde{B} = B - B_s. \quad (28)$$

It leads to a modified version of Equation (15) for the magnetic field evolution,

$$\left(1 + \frac{\mu_B}{\mu}\right) \dot{B} = -i\partial_z \left(D \partial_z B\right) + \frac{B_z^2}{4\pi\mu} \dot{B}_s + B_z \partial_z \dot{\xi}_{\rm pl}. \quad (29)$$

Plastic flows are triggered where $\tilde{B}$ exceeds $B_{\rm cr}$, and $\tilde{B}$ should replace B in the equation of plastic flow dynamics. Therefore, Equation (19) is replaced by

$$B_z \partial_z \dot{\xi}_{\rm pl} = -\alpha \tilde{B} \left(1 - \frac{B_{\rm cr}^{\rm new}}{|\tilde{B}|}\right) \Theta\left(|\tilde{B}| - B_{\rm cr}^{\rm new}\right). \quad (30)$$

To close the set of equations describing the system, one must specify the evolution of B_s. It is controlled by two factors: (1) B_s is pumped by the crustal motions. (2) The external twist has a finite lifetime, because it requires a magnetospheric current $\mathbf{j} = (c/4\pi)\nabla \times \mathbf{B} \neq 0$. For instance, in the axisymmetric geometry $B_s \neq 0$ would be a toroidal field which requires a poloidal magnetospheric current (Thompson et al. 2002). The current is sustained through $e^{\pm}$ discharge with a threshold voltage that regulates the damping time of the external twist to ~ 1 yr (Beloborodov & Thompson 2007).

The pumping of B_s by crustal motions can be implemented in our one-dimensional model as shown in Figure 5. We consider a magnetosphere with a constant vertical magnetic field B_z and a constant horizontal field B_s that serves as a proxy for the twist component in three dimensions. The pumping of B_s is caused by the motion of magnetic field lines at the crust surface. This motion can be related to the evolution of $B(z,t)$ inside the crust by integrating Equation (5) from the bottom to the top of the crust,

$$\int_{\rm bottom}^{\rm surface} {\rm d}z \, \frac{\dot{B}}{B_z} = (v + \eta \partial_z B)\Big|_{\rm bottom}^{\rm surface}, \quad (31)$$

where $v(z,t) = v_H + \dot{\xi} = v_x + i v_y$ is the velocity vector of the electron fluid. Neglecting the lattice deformation at the base of the crust, $\dot{\xi}_{\rm bottom} = 0$, we get the surface velocity of the magnetic field lines,

$$v_s = \int_{\rm bottom}^{\rm surface} {\rm d}z \, \frac{\dot{B}}{B_z} + (v_H + \eta \partial_z B)_{\rm bottom}. \quad (32)$$

Here we kept the resistive term $\eta \partial_z B$ at the bottom (because the typical setup of our simulations has a strong current sheet at the bottom), and neglected $\eta \partial_z B$ at the surface, as its effect on the evolution of B_s will be small compared to ohmic dissipation in the magnetosphere. The magnetic field at the surface follows the motion of the electron fluid with velocity v_s.

The rate of pumping B_s is proportional to v_s, and the evolution equation for B_s may be written in the form,

$$\dot{B}_s = -B_z \frac{v_s}{L} - \frac{B_s}{\tau_{\rm damp}}. \quad (33)$$

Here L represents the length of the magnetospheric field lines (Figure 5) and $\tau_{\rm damp}$ is the damping timescale. In a complete model, the value of $\tau_{\rm damp}$ would depend on the voltage of $e^{\pm}$ discharge in the magnetosphere and the geometry of the twisted bundle of field lines (Beloborodov 2009). In our simplified model we fix $\tau_{\rm damp} = 1$ yr.

The Hall evolution at the bottom boundary is slow and not capable of pumping B_s against the twist damping in the magnetosphere. However, significant external twists can be created as a result of the large $\dot{B}$ in the regions of plastic failures (Beloborodov & Levin 2014).

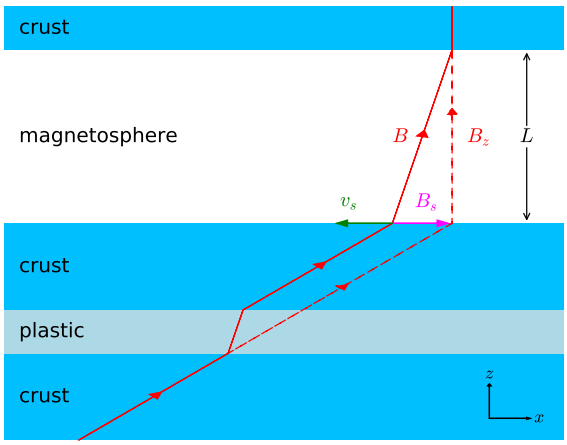

FIG. 5.— Illustration for the magnetic field lines in the crust (blue region) and in the magnetosphere (white region). A closed magnetic field line is anchored between two footpoints in the crust. The plot is projected in the direction of magnetic field line. Plastic flow occurs in the light blue region and results in a crustal surface motion with velocity v_s. This motion shears the magnetosphere and creates B_s. Red dashed and solid lines are the magnetic field line before and after the plastic deformation.

6. GLOBAL SIMULATION

6.1. *Setup*

We now collect all the ingredients described in the previous sections into a global simulation of the magnetic field evolution in a magnetar crust over 10 kyr. The crust will now have a realistic density profile $\rho(z)$. Its temperature profile $T(z)$ is calculated self-consistently by evolving the time-dependent equation for heat transfer,

$$C_V \dot{T} = \partial_z \left(\kappa \partial_z T\right) + q_{\rm pl} + q_{\rm ohm} - q_\nu. \qquad (34)$$

It takes into account the plastic heating (Equation 21), the ohmic heating $q_{\rm ohm} = (\eta/4\pi)|\partial_z B|^2$, and the energy losses due to neutrino emission q_ν.

The coupled evolution of $B(z,t)$ and $T(z,t)$ in the crust, and $B_s(t)$ at the surface, is followed by solving Equations (29), (34), (32), and (33); Equation (30) is used where plastic flows occur.

While our one-dimensional model can only approximate the behaviour of a real magnetar, it allows one to use a realistic vertical profile for all of the important physical parameters of the crust. We use the BSK20 model provided by Potekhin et al. (2013) to compute the density ρ, electron number density n_e, nuclear charge Z and mass A as a function of depth z. The mass of the neutron star is chosen to be $1.4M_\odot$, for which the model predicts the radius of 11.7 km. The shear modulus μ is calculated using the fitting formula provided by Piro (2005) and Sotani et al. (2007) for low and high densities. To accelerate the computations, in most of our runs the ohmic diffusivity is set to $\eta = |D_H|/20$, the value which is characteristic for the inner crust. We have separately checked that the details of ohmic dissipation do not affect our results, as most of the energy is dissipated in the plastic flow regions. Our fiducial value for the vertical magnetic field is $B_z = 3\times10^{14}$ G, which is a typical poloidal field of magnetars inferred from their spindown rates.

We choose the upper boundary of our simulation domain at $z = z_b$ where $\rho_b \equiv \rho(z_b) = 10^9$ g/cm^3. Our results are not sensitive to this choice so long as (1) the crustal shear modulus at the boundary is sufficiently weak, $\mu(\rho_b) \ll B_z^2/4\pi$, and (2) the timescale of heat conduction from the boundary to the stellar surface $t_c(\rho_b)$ is much shorter than the typical conduction time across the crust, which is comparable to one year. The choice of $\rho_b = 10^9$ g/cm^3 gives $4\pi\mu(\rho_b)/B_z^2 \sim 10^{-4}$ and $t_c(\rho_b) \sim 10^6$ s for typical magnetar temperatures. Our computational box includes the entire crust at $\rho > \rho_b$, which has a thickness of about 1 km. We use 30,000 evenly spaced grid points; this gives enough resolution for capturing small-scale Hall waves.

We employ the Crank-Nicolson scheme (Press 2007) to solve both the Hall wave propagation and the thermal evolution. In our fiducial run, we keep a constant horizontal magnetic field $B_{\rm core} = 6\times10^{15}$ G at the lower crust boundary $z_{\rm core}$. The horizontal field at the upper boundary B_s evolves dynamically according to Equation (33), which provides a time-dependent boundary condition at ρ_b. The initial condition for the horizontal field B is chosen to be

$$B(z) = B_{\rm core} \exp\left[-\frac{(z-z_{\rm core})^2}{l^2}\right], \qquad z_b < z < z_{\rm core}, \qquad (35)$$

with $l = 10$ m. Thus, initially the crust has practically no horizontal field, and the presence of a strong horizontal field at the boundary launches Hall waves into the crust as described in Section 2.1. The exact value of $l \ll 100$ m has no impact on the model's long-term behavior. We envisage that this type of initial configuration may result from a quick rearrangement of the core magnetic field.

It is important for our purposes to accurately track the thermal evolution of the crust. We choose the initial surface temperature to be $T_{s0} = 2\times10^6$ K which is typical for transient magnetars in quiescence. The initial temperature profile below the surface sustains the steady heat flux $F = -\kappa\partial_z T = \sigma_{\rm SB} T_{s0}^4$ conducted from the core. The corresponding temperature of the core and the lower crust is $\sim 3\times10^8$ K. Neutrino cooling is negligible at such temperatures, however it becomes important later when the crust is heated by the avalanches of Hall waves and thermoplastic waves. For simplicity, the core temperature is kept constant throughout the simulation. This may be reasonable due to the high heat capacity of the core, and this also assumes that the main phase of its intrinsic thermal evolution occurred at earlier times, see Beloborodov & Li (2016). The temperature profile of the heated crust is evolved by solving the time-dependent heat transfer equation as described in Li & Beloborodov (2015). We use the code provided by Potekhin (1999) to calculate C_V and κ in the strong magnetic field. At high temperatures, the crust is efficiently cooled by neutrino emission. Several processes contribute to the neutrino emissivity q_ν; our simulations include the effects of annihilation of electron-positron pairs, plasmon decay, neutrino bremsstrahlung, and neutrino synchrotron emission. We use the formulae provided in Yakovlev et al. (2001) to calculate q_ν from all these channels.

The Hall wave propagation is typically slow compared to plastic instabilities and heat propagation. Therefore,

the timestep in our simulations is adaptive and chosen to resolve the fastest processes when they happen — the plastic flows, neutrino cooling, and twisting of the external magnetosphere. We require that the local temperature change due to plastic heating or neutrino emission in one timestep does not exceed 10^7 K and the change in B_s is smaller than 10^9 G. To speed up the calculation, we track the thermal evolution only when there is an episode of plastic heating until the temperature profile has relaxed back to the steady heat flow from the core (i.e. when the temperature profile is everywhere close to the initial state, with deviations smaller than 10^7 K). When the thermal evolution is turned off, the timestep is set at 5×10^4 s. We have tested that it is short enough to resolve the Hall wave propagation in the absence of plastic failures. We use $\alpha = 10^{-4}$ s^{-1} and run our simulation to 10 kyr. The energy conservation is better than 1% during the whole simulation for Hall wave evolution and 5% for thermal evolution.

When no plastic failure is triggered, the crust is only heated by ohmic dissipation. Its effect on temperature is however small, $\Delta T < 10^7$ K. When a plastic failure occurs, the local plastic heating greatly exceeds the ohmic heating. Therefore, we neglect the contribution of ohmic heating in the thermal evolution equation at all times. However, ohmic damping is taken into account in the Hall evolution equation for the magnetic field, where its effect is more significant.

As explained in Section 3, an important element of our model is the dependence of the critical shear stress on temperature (the thermal softening of the crust). We use the expression given in Equation (17) as long as there is no plastic failure. When the plastic flow is initiated, at failed sites the maximal shear stress supported by the crust drops to $\sigma_{\rm cr}^{\rm new}$, 10% of its original value at zero temperature; this corresponds to the reduction of $B_{\rm cr}$ by a factor of 10 (see Section 3.2). The crustal lattice heals when $|B-B_s|B_z/4\pi$ approaches $\sigma_{\rm cr}^{\rm new}$, which occurs on the timescale of $3000/\alpha \sim 1$ year. At this point, the critical shear stress is increased back to the value given by Equation (17). If the strong local heating melts the crust, then $\sigma_{\rm cr}$ vanishes and the local B must immediately relax to B_s, releasing magnetic energy. The dynamics of this fast process is not resolved in our simulations, instead we simply allow $B-B_s$ to be exponentially reduced on the timescale α^{-1} and convert the released magnetic energy to heat.

6.2. *Results*

Figure 6 shows the initial Hall evolution, which gradually fills the crust with a horizontal magnetic field. The field eventually triggers plastic failures, which launch new Hall waves, and then the evolution continues in a chaotic manner, with repeating thermoplastic waves and Hall-mediated avalanches at various locations in the crust.

The spacetime diagram in Figure 7 shows failure development during a major Hall-mediated avalanche at $z \approx 0.5$ km, which propagates into the deeper crust and concludes with a strong thermoplastic wave at $z = 0.6-0.67$ km. The duration of the avalanche is about one year. A significant magnetic and elastic energy is dissipated during this time through the friction in the plastic flow (crustal ohmic heating makes a negligible contribution). The evolution of heating and neutrino cooling

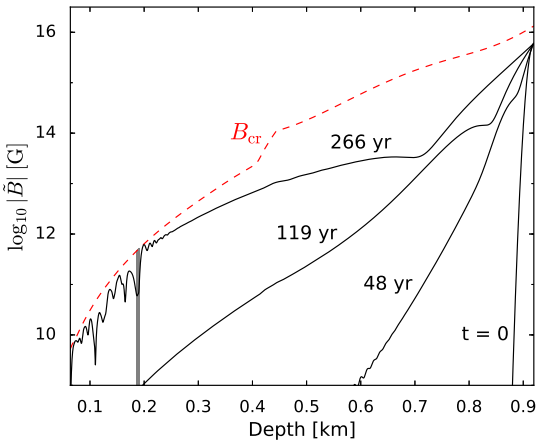

FIG. 6.— Snapshots of the magnetic field evolution, showing how the horizontal magnetic field B gradually fills the crust from its lower boundary at $z \approx 1$ km. The horizontal axis shows the depth of the crust. The neutron star surface is to the left and core-crust interface is on the right where Hall waves are launched. Solid curves show $|\tilde{B}| = |B - B_s|$ vs. depth z. $B_s \neq 0$ corresponds to the external magnetospheric twist; it is negligible at most times, except when the magnetosphere is quickly twisted by the plastic instabilities of the crust. Such motions are triggered when $\tilde{B}$ approaches $B_{\rm cr}$ (shown by the dashed red curve). This is seen to happen in the snapshot at $t = 266$ yr; the plastically flowing region at $z \sim 0.2$ km is indicated by the vertical grey strip. $B_{\rm cr}$ is calculated at the steady-state temperature profile that corresponds to the surface temperature of 2×10^6 K.

(integrated over depth z) is shown in the lower panel of Figure 8. A fraction of the produced heat is conducted to the stellar surface, increasing its luminosity. The evolution of the surface radiation flux is shown in the upper panel of Figure 8; it is rather smooth, because the characteristic timescale for heat conduction is comparable to one year.

The developing avalanche shears the stellar surface and pumps magnetic energy into the magnetosphere. This energy is gradually dissipated through the continual $e^{\pm}$ discharge in the magnetosphere, producing radiation that is also shown in the upper panel of Figure 8. The magnetospheric activity rises slowly during the Hall-mediated phase, and jumps upward when the strong thermoplastic wave occurs in the end of the avalanche. This last event is quick and suddenly implants a significant twist into the magnetosphere. After that, the magnetospheric emission decays resistively on the timescale of a year. Neutrino emission also peaks during the strong thermoplastic wave, because the temperature is highest at this stage, and neutrino emission is extremely sensitive to temperature.

Figure 9 shows another failure at $z \sim 0.5$ km at a later time during the evolution. This time, $\tilde{B}$ closely approached $B_{\rm cr}$ in a broader range of depths, and the failure immediately triggers a giant thermoplastic wave, which propagates from $z \approx 0.5$ km to 0.85 km. It travels much faster and a longer distance compared with the Hall-mediated avalanche in Figure 7. The temperature is higher and there is a strong temperature gradient across the wave front, which sustains its propagation.

Thermoplastic wave is a fast mode of failure propagation compared with the Hall-mediated avalanche; in this

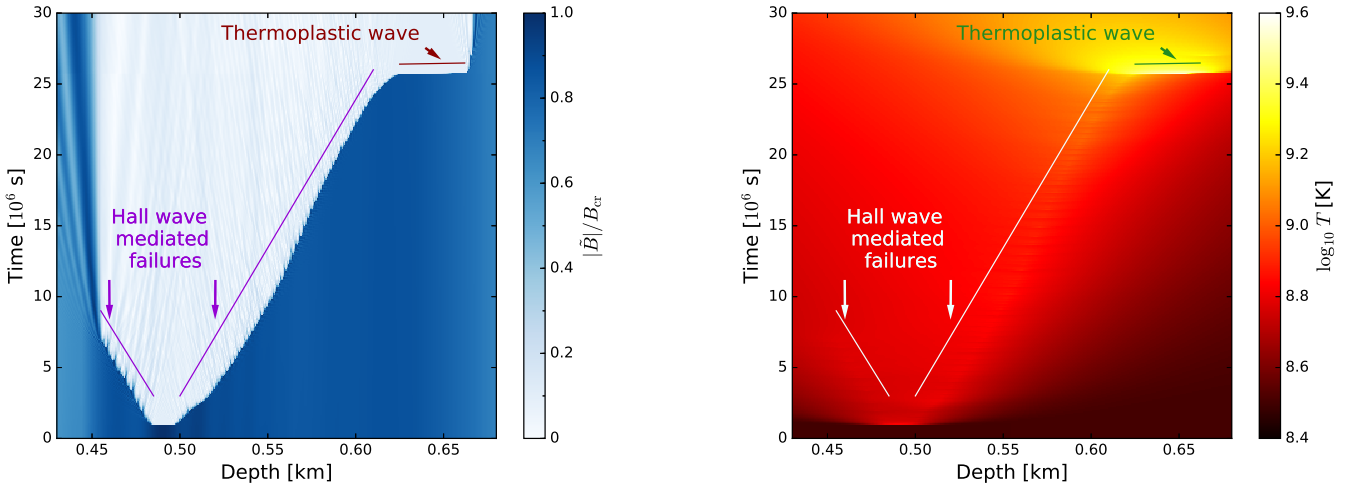

FIG. 7.— Spacetime diagram for failure generation and propagation in the crust. **Left panel:** evolution of $|\tilde{B}|/B_{\rm cr}$. At the failure sites, the value of $|\tilde{B}|/B_{\rm cr}$ drops to 0.1 which corresponds to the pale blue color. The magnetic stresses in the neighborhood of the first failures (which are about 20 m thick) are not able to launch large thermoplastic waves. Instead, propagation of the initial failures is assisted by short Hall waves. When the Hall-mediated avalanche reaches the depth of 0.6 km, a strong thermoplastic wave is launched, which propagates much faster and quickly reaches $z \approx 0.67$ km, where the wave extinguishes. **Right panel**: Temperature evolution. Before the failure is triggered the temperature is kept near the initial steady state. As the failure develops, plastic heating increases the temperature. The heating is particularly strong in the thermoplastic wave developing at $z \approx 0.6$ km.

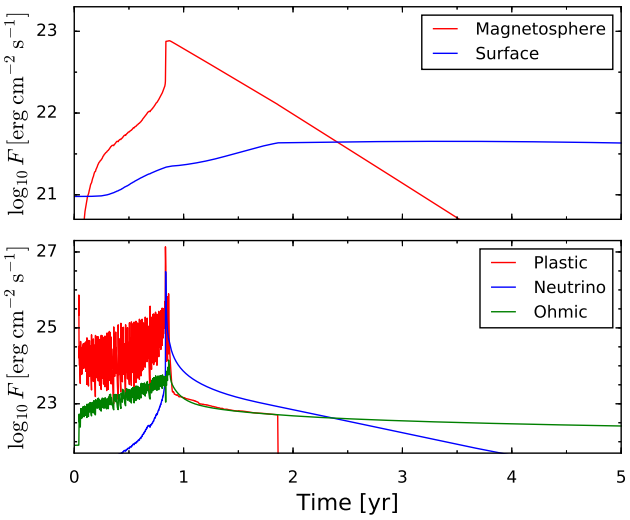

FIG. 8.— **Upper panel:** radiation flux from the stellar surface (blue) and dissipation rate in the magnetosphere per unit area of the crust (red). **Lower panel:** vertically integrated rates of plastic heating (red), ohmic heating (green), and neutrino cooling (blue), during and after the failure avalanche shown in Figure 7.

example its duration is only 0.02 year (7×10^5 s). It produces fast and strong heating of the crust and twisting of the external magnetosphere (Figure 10). However, the resulting radiation flux from the stellar surface is not much higher than in Figure 8. This is because heat is deposited deeper in the crust, and a larger fraction of the heat is conducted into the core and lost to neutrinos. This is in agreement with the behavior seen in Kaminker et al. (2006, 2014), see Beloborodov & Li (2016) for a discussion of the surface heating efficiency.

Figure 11 shows the evolution of surface displacement in the x and y directions during our entire simulation. The displacement is zero at the beginning, before the Hall wave launched at the crust-core interface reaches the surface. Each failure event causes the displacement to change abruptly. The large abrupt jump in the displacement near 3 kyr is the result of the giant thermoplastic wave shown in Figure 9. The smaller jump near 7 kyr corresponds to the event shown in Figure 7. There is another large jump of 1.5 km caused by the thermoplastic wave at $t \approx 9$ kyr.

Figure 12 shows the evolution of observable radiation, from the surface and the magnetosphere, during the entire simulation. Both magnetospheric and surface emissions occur in sporadic spikes. There seems to be no obvious pattern for the spikes. Each spike is an outburst caused by thermoplastic waves or Hall-mediated failures or a combination of both. The two large thermoplastic waves at 3 kyr and 9 kyr produce the strongest magnetospheric emission.

Figure 13 shows the evolution of the column density of "free" energy W (density integrated over z) stored in the crust and available for dissipation; it includes the energy of the horizontal magnetic field and the elastic deformation energy. The figure also shows the contributions to the changes in W due to the Poynting flux from the core, plastic and ohmic dissipation, neutrino losses, the Poynting flux into the magnetosphere and heat flux radiated away at the surface above the persistent background. Whenever there is an outburst, the free energy of the crust drops while the produced (time-integrated) heat, neutrino and radiative losses rapidly increase. Plastic and ohmic dissipation are the two main channels by which the crust is heated, with most of the heat lost to neutrinos or conducted into the core. While the plastic heating only happens sporadically, the ohmic heating takes place continuously at a much lower rate and has a negligible effect on the temperature change and emerging flux during the outburst. Only a small part of the dissipated energy (about 1%) is injected and damped through the magnetospheric twist decay, and an even smaller part

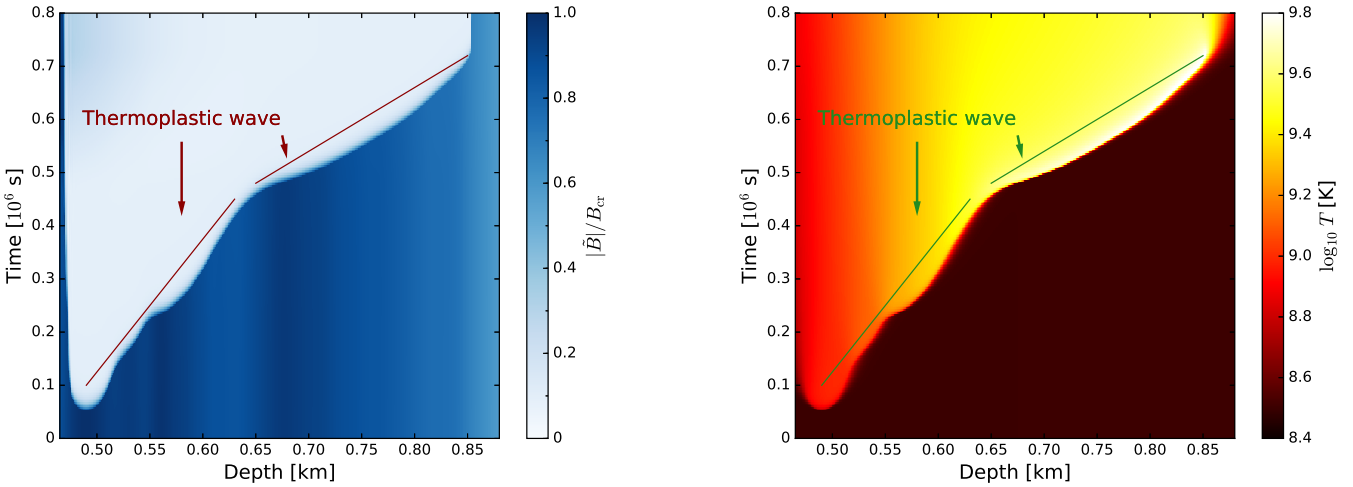

FIG. 9.— Spacetime diagram for a giant thermoplastic wave observed in the simulation at $t \approx 3.2$ kyr. **Left panel:** evolution of $\tilde{B}/B_{\rm cr}$. Note the smaller scale on the time axis compared with Figure 7; the thermoplastic wave is much faster than the Hall-mediated avalanche. **Right panel:** temperature evolution. Compared to Figure 7, the heating is stronger and occurs deeper in the crust. There is also a strong temperature gradient across the wave front.

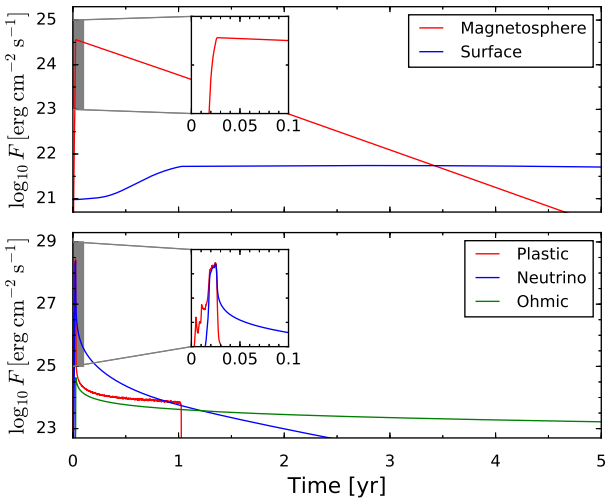

FIG. 10.— **Upper panel:** radiation flux from the stellar surface (blue) and dissipation rate in the magnetosphere per unit area of the crust (red). The insets zoom into the initial spike at the time of the thermoplastic wave. **Lower panel:** vertically integrated rates of plastic heating (red), ohmic heating (green), and neutrino cooling (blue), during and after the thermoplastic wave shown in Figure 9.

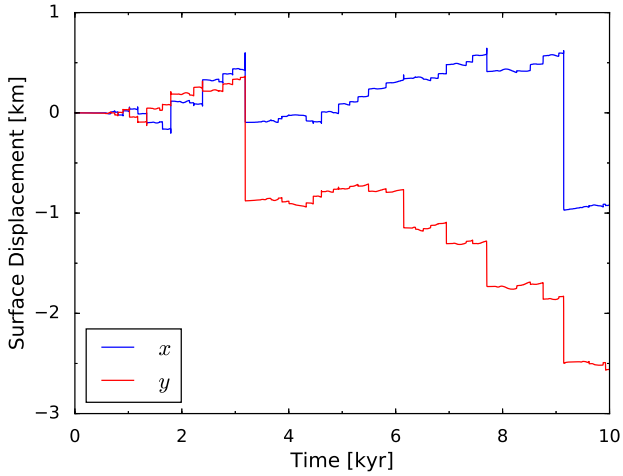

FIG. 11.— Evolution of surface displacement in the horizontal x and y directions during the entire 10 kyr simulation.

reaches the surface through heat diffusion. It is through these two channels that the outburst produces the observable X-ray luminosity.

7. DISCUSSION

Hall evolution of the magnetic field provides a robust mechanism for growing magnetic stress in the solid crust of a magnetar, and yielding to theses stresses results in mechanical heating of the crust. Beloborodov & Li (2016) showed that heating from internally fostered crustal failures obeys strong constraints, which prevent it from sustaining the observed high temperatures of persistently luminous magnetars. In agreement with these constraints, our results do not show a strong persistent heating of magnetars. However, the described mechanism of activity driven by Hall drift can have significant observational implications. The intermittent shear motions of the failed crust play a key role for twists of the external magnetosphere and also provide sporadic mechanical heating. This may explain outbursts of activity, in particular in the increasing number of so-called transient magnetars.

The model we have studied is one-dimensional, and therefore can only serve as a proxy for the evolution of magnetic fields and crustal deformations of real three-dimensional magnetars. However, we expect that the main features of the model, i.e. the avalanches of mechanical failures mediated by short wavelength Hall waves, large-scale thermoplastic waves, and the magnetospheric twists that these cause, will be present in a more realistic three-dimensional dynamics. We note also that multidimensional simulations will likely show the interaction of crustal failures with the non-linear Hall dynamics that is not captured in our 1D model. Magnetic

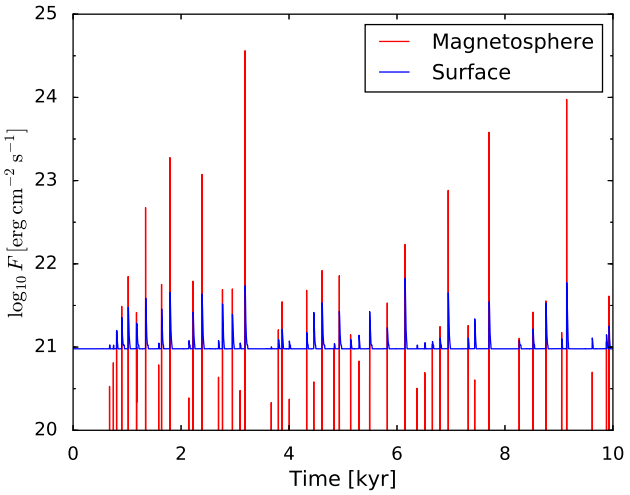

FIG. 12.— Evolution of the radiation flux from the stellar surface (blue) and dissipation rate in the magnetosphere per unit area of the crust (red) during the entire 10 kyr simulation.

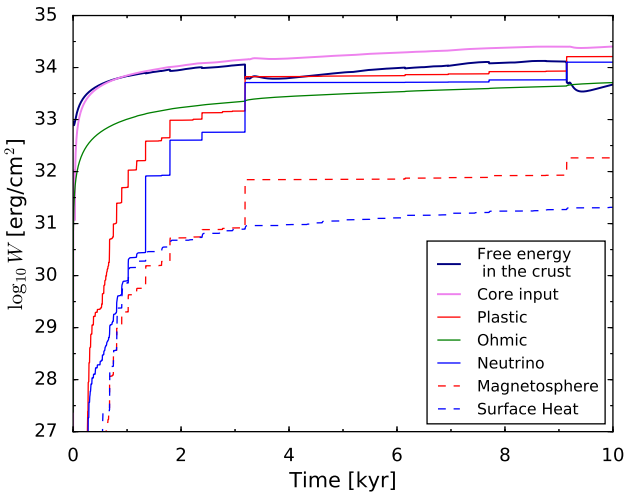

FIG. 13.— Evolution of the free energy stored in the crust and the contributions to its changes (see text).

instabilities in 2D or 3D, e.g. density-shear instability (**??**), will provide other channels to launch Hall waves by creating current sheets in the crust (**?**). In what follows we comment on how the simulated outbursts in our model compare with the observed outbursts.

During an outburst of a transient magnetar the observed X-ray flux increases by a factor of 10-1000 compared to its quiescent level and typically decays on the time scale of months to years. A canonical example is provided by the first discovered transient magnetar XTE J1810-197 (Ibrahim et al. 2004), with the characteristic dipole magnetic field $\sim 3\times10^{14}$ G. It was discovered in January 2003 when its X-ray luminosity was comparable to 10^{35} erg s^{-1}, which is a factor of ~ 100 above the quiescent level. It returned back to the quiescent level in a few years (Gotthelf & Halpern 2007). However, no data is available for the early phase of this event (from Nov. 2002 to Jan. 2003) and so one cannot observationally study the rise of its light curve. The spectral fits of the outburst showed the appearance and subsequent shrinking of a hot spot on the star of size $\lesssim 3$ km, which indicates a localized twist of the external magnetosphere. The transient magnetar discovered recently in the Galactic Centre SGR 1745−2900 (Kennea et al. 2013; Mori et al. 2013) is almost a twin of XTE J1810-197. Its outburst showed a similar decay, with a similar shrinking hot spot (Kaspi et al. 2014; Coti Zelati et al. 2015). Similar strong outbursts were observed in several other transient magnetars (see Rea & Esposito (2011) for a review).

Less dramatic outbursts are also observed in "persistent" magnetars that show a continuously high level of emission during decades of observations. For instance, the long-term observations of 1E 1048.1-5937 captured four outbursts (and resolved their rise times) between 2001 and 2007 (Tam et al. 2008). The 2001-2002 event increased the X-ray luminosity by a factor of ~ 2 over ~ 20 days and then decayed over $\sim$100 days (Gavriil & Kaspi 2004). The rise times of the 2002 and 2004 outbursts were a few weeks. The 2007 outburst rose to its peak in less than a week (Tam et al. 2008).

How does this data stack up against our model? The model predicts spikes in surface radiation flux of $10^{22}-10^{24}$ erg s^{-1} cm^{-2}. Assuming an emission area of about 10^{11}cm^2 (3 km $\times$ 3 km), our simulated peaks of luminosity are $10^{33}-10^{35}$ erg/s. The typical decay time of luminosity after the end of the failure event is typically comparable to one year. These values are in good agreement with observations.

In our model, we have three different timescales: the timescale of thermoplastic waves (controlled by parameter α), Hall-mediated avalanches, and heat diffusion. The heat diffusion timescale is comparable to one year and independent of the plastic-flow constant α. It controls both the rise and the decay of surface luminosity due to heat diffusion from the heated interior to the surface. The observed rise times in the sources described above are often much shorter, more consistent with the timescale of magnetospheric twisting by thermoplastic waves. This suggests that the onset of the outburst is controlled by magnetospheric dissipation induced by the plastic motions of the crust. These motions extract energy from the stellar interior (through Poynting flux) much faster than heat diffusion, and with a higher efficiency. A significant fraction of energy dissipated in the magnetosphere should be delivered to the surface by accelerated particles and radiated from the surface. There is strong observational evidence for this external heating of the magnetar surface, see Beloborodov & Li (2016).

Our simulation shows that the outburst rise time depends on whether the crustal failure develops through a Hall-mediated avalanche or a large-scale thermoplastic wave. The rate of crustal failure (and the corresponding surface shear rate) in both cases is proportional to $\alpha^{1/2}$, see Equations (22) and (26), and their ratio is independent of α. The Hall-mediated avalanche is slower by the factor of $(D_{\rm H}/\chi)^{1/2}$, where $D_{\rm H}=(cB_z/4\pi en_e)$ is the Hall diffusion coefficient and $\chi=\kappa/C_V\sim 10-100$ cm^2 s^{-1} is the heat diffusion coefficient. The factor $(D_{\rm H}/\chi)^{1/2}$ is typically around 10^{-2}. The value of α is unknown, and both failure modes can be fast, giving short outburst rise times. For the choice of param-

eters in our simulations, $\alpha = 10^{-4}$ s^{-1}, the typical outburst light-curve from a thermoplastic wave rises to its peak in days to weeks. The decay occurs on the much longer timescales of resistive magnetospheric untwisting and heat diffusion through the crust. Both of these timescales are known to be roughly comparable to one year.

In our simulation, we see a large outburst every several hundred years. However, our simple 1D model simulates only a small patch on the magnetar surface — our simulation box may represent a crustal plate with surface area of a few square kilometers (as the crust thickness is about one kilometer). There may be hundreds of such independent patches, each undergoing its own series of outbursts. 2D or 3D simulations will be required to model the global picture, which can give much more frequent outbursts. The outburst rate also increases with increasing $B_{\rm core}$. Our simulations assumed $B_{\rm core} = 6 \times 10^{15}$ G, and a higher value would increase the magnetic energy flux from the core into the crust and make it easier to initiate plastic failures in the deeper crust.

In this paper we concentrated on the relatively slow dynamics of outbursts. Therefore our results do not directly apply to the distinct class of magnetar bursts and flares that have much shorter durations, with rise times much shorter than one second. Thompson & Duncan (1995, 1996) proposed that the bursts result from sudden "brittle" failures in the crust. It is, however, unclear how the compressed magnetized material with pressure well above the Coulomb lattice energy could be brittle (Jones 2003; Levin & Lyutikov 2012; Beloborodov & Levin 2014). Therefore, it appears more likely that the fast flares result from explosive relaxation of the twisted magnetosphere (Thompson & Duncan 1995; Lyutikov 2006; Parfrey et al. 2012, 2013). These magnetospheric explosions also produce sudden deformations of the crust (Li & Beloborodov 2015) which leave strong gradients in the crustal magnetic field and may be followed by accelerated Hall evolution. Both "internal" (brittle) and "external" (magnetospheric) models could be related to the clusters of "storm bursts" (Götz et al. 2006; Israel et al. 2008, 2010; Scholz & Kaspi 2011) if the Hall evolution induced by a burst leads to more bursts.

The avalanches of thermoplastic failures and heating of the crust may affect the rotation rate of the magnetar by changing the rotation of the neutron superfluid in the lower crust. The superfluid vortices could become unpinned from the crustal lattice, resulting in timing anomalies — glitches or anti-glitches associated with outbursts. We defer the study of this possibility to future work.

This work was supported by a Monash Research Acceleration grant, NASA grant NNX13AI34G, and a grant from the Simons Foundation (#446228, Andrei Beloborodov).

REFERENCES

Beloborodov, A. M. 2009, ApJ, 703, 1044
—. 2013, ApJ, 777, 114
Beloborodov, A. M., & Levin, Y. 2014, ApJ, 794, L24
Beloborodov, A. M., & Li, X. 2016, ArXiv e-prints, arXiv:1605.09077
Beloborodov, A. M., & Thompson, C. 2007, ApJ, 657, 967
Chugunov, A. I., & Horowitz, C. J. 2010, MNRAS, 407, L54
Coti Zelati, F., Rea, N., Papitto, A., et al. 2015, MNRAS, 449, 2685
Cumming, A., Arras, P., & Zweibel, E. 2004, ApJ, 609, 999
Gavriil, F. P., & Kaspi, V. M. 2004, ApJ, 609, L67
Goldreich, P., & Reisenegger, A. 1992, ApJ, 395, 250
Gotthelf, E. V., & Halpern, J. P. 2007, Ap&SS, 308, 79
Gotthelf, E. V., Halpern, J. P., Buxton, M., & Bailyn, C. 2004, ApJ, 605, 368
Götz, D., Mereghetti, S., Molkov, S., et al. 2006, A&A, 445, 313
Gourgouliatos, K. N., & Cumming, A. 2014, MNRAS, 438, 1618
—. 2015, MNRAS, 446, 1121
Gourgouliatos, K. N., Cumming, A., Reisenegger, A., et al. 2013, MNRAS, 434, 2480
Hascoët, R., Beloborodov, A. M., & den Hartog, P. R. 2014, ApJ, 786, L1
Hollerbach, R., & Rüdiger, G. 2004, MNRAS, 347, 1273
Horowitz, C. J., & Kadau, K. 2009, Physical Review Letters, 102, 191102
Ibrahim, A. I., Markwardt, C. B., Swank, J. H., et al. 2004, ApJ, 609, L21
Israel, G. L., Romano, P., Mangano, V., et al. 2008, ApJ, 685, 1114
Israel, G. L., Esposito, P., Rea, N., et al. 2010, MNRAS, 408, 1387
Jones, P. B. 2003, ApJ, 595, 342
Kaminker, A. D., Kaurov, A. A., Potekhin, A. Y., & Yakovlev, D. G. 2014, MNRAS, 442, 3484
Kaminker, A. D., Yakovlev, D. G., Potekhin, A. Y., et al. 2006, MNRAS, 371, 477
Kaspi, V. M., Archibald, R. F., Bhalerao, V., et al. 2014, ApJ, 786, 84
Kennea, J. A., Burrows, D. N., Kouveliotou, C., et al. 2013, ApJ, 770, L24
Kojima, Y., & Kisaka, S. 2012, MNRAS, 421, 2722
Levin, Y., & Lyutikov, M. 2012, MNRAS, 427, 1574
Li, X., & Beloborodov, A. M. 2015, ApJ, 815, 25
Lyutikov, M. 2006, MNRAS, 367, 1594
—. 2015, MNRAS, 447, 1407
Mereghetti, S. 2008, A&A Rev., 15, 225
Mori, K., Gotthelf, E. V., Zhang, S., et al. 2013, ApJ, 770, L23
Parfrey, K., Beloborodov, A. M., & Hui, L. 2012, ApJ, 754, L12
—. 2013, ApJ, 774, 92
Perna, R., & Pons, J. A. 2011, ApJ, 727, L51
Piro, A. L. 2005, ApJ, 634, L153
Pons, J. A., & Rea, N. 2012, ApJ, 750, L6
Potekhin, A. Y. 1999, A&A, 351, 787
Potekhin, A. Y., Fantina, A. F., Chamel, N., Pearson, J. M., & Goriely, S. 2013, A&A, 560, A48
Press, W. H. 2007, Numerical recipes 3rd edition: The art of scientific computing (Cambridge university press)
Rea, N., & Esposito, P. 2011, Astrophysics and Space Science Proceedings, 21, 247
Scholz, P., & Kaspi, V. M. 2011, ApJ, 739, 94
Sotani, H., Kokkotas, K. D., & Stergioulas, N. 2007, MNRAS, 375, 261
Tam, C. R., Gavriil, F. P., Dib, R., et al. 2008, ApJ, 677, 503
Thompson, C., & Duncan, R. C. 1995, MNRAS, 275, 255
—. 1996, ApJ, 473, 322
Thompson, C., Lyutikov, M., & Kulkarni, S. R. 2002, ApJ, 574, 332
Viganò, D., Rea, N., Pons, J. A., et al. 2013, MNRAS, 434, 123
Wood, T. S., & Hollerbach, R. 2015, Physical Review Letters, 114, 191101
Woods, P. M., & Thompson, C. 2006, Soft gamma repeaters and anomalous X-ray pulsars: magnetar candidates, ed. W. H. G. Lewin & M. van der Klis, 547–586
Yakovlev, D. G., Kaminker, A. D., Gnedin, O. Y., & Haensel, P. 2001, Phys. Rep., 354, 1